ACCSCIENCE PUBLISHING

International Journal of Bioprinting

RESEARCH ARTICLE

Structural design and multiphase biomechanical evaluation of a topology-optimized metal 3D-printed dual-compression plate for patellar fractures

Chi-Yang Liao[1,2], Shao-Fu Huang[3,4], Ya-Han Chan[4], Hsuan-Wen Wang[3,4], Yu-Pin Yang[4], and Chun-Li Lin[3,4]*

[1]Department of Orthopedics, Tri-Service General Hospital Songshan Branch, National Defense Medical University, Taipei, Taiwan

[2]Department of Surgery, Tri-Service General Hospital Songshan Branch, National Defense Medical University, Taipei, Taiwan

[3]Department of Biomedical Engineering, Innovation & Translation Center of Medical Device, National Yang Ming Chiao Tung University, Taipei, Taiwan

[4]Department of Biomedical Engineering, National Yang Ming Chiao Tung University, Taipei, Taiwan

(This article belongs to the *Special Issue*: *3D Printing for Advancing Orthopedic Applications*)

Abstract

Patellar fractures, especially transverse and comminuted types, often present mechanical challenges that exceed the capabilities of conventional fixation constructs. This study develops a topology-optimized metal three-dimensional-printed dual-compression patellar plate designed to improve fragment stability while maintaining appropriate intraoperative rigidity. The plate design was first refined using an original anatomically assembled thin bone plate, which underwent finite element analysis and topology optimization to preserve primary load-bearing paths and reduce excessive stiffness. The optimized structure was subsequently fabricated using selective laser melting with Ti-6Al-4V and mechanically evaluated in accordance with American Society for Testing and Materials F382 standards. Static four-point bending tests demonstrated a proof load (P) of 257.31 ± 5.40 N and structural bending stiffness of 1.10 ± 0.01 N·m^2. Fatigue testing revealed runout at 15% *P*, while failure occurred at higher load levels (25% *P* & 30% *P*), revealing two distinct modes: plate fracture at topology-optimized transition zones and locking-screw shear failure. Static tensile testing revealed that dual-compression fixation significantly ($p<0.05$) enhanced load-bearing capacity compared with single-compression fixation for both C1 (712 N vs. 517.5 N) and C3 (253.75 N vs. 205.25 N) fracture models. Dynamic knee-extension testing demonstrated that dual compression markedly reduced medial–lateral fracture micromotion, decreasing C3 gaps from 0.348–0.534 mm to 0.078–0.107 mm without increasing quadriceps reaction force. Overall, the topology-optimized dual-compression patellar plate provides mechanically validated interfragmentary stability, effective micromotion control, and a well-defined fatigue performance envelope, supporting its potential as an advanced fixation solution for clinically challenging patellar fractures.

Keyword: Biomechanics; Dynamic tests; Four-point bending; Patella; Three-dimensional printing

***Corresponding author:**
Chun-Li Lin
(cllin2@nycu.edu.tw)

Citation: Liao CY, Huang SF, Chan YH, Wang HW, Yang YP, Lin CL. Structural design and multiphase biomechanical evaluation of a topology-optimized metal 3D-printed dual-compression plate for patellar fractures. *Int J Bioprint*. 2026;12(1):689-706. doi: 10.36922/IJB025480494

Received: November 25, 2025
Revised: December 14, 2025
Accepted: December 26, 2025
Published online: January 8, 2026

1. Introduction

Patellar fractures account for approximately 0.5–1.5% of all fractures, primarily caused by direct impact or forceful quadriceps contraction.[1–8] Integrity of the patella is crucial for knee stability and lower limb movement due to its location at the lever center of the knee extensor system. Additionally, it plays a crucial role in transmitting pressure and tension between the quadriceps and patellar tendon.[1–8] Although traditional tension band wiring fixation can withstand tensile stress, it struggles to provide sustained and effective compression across the fracture interface. Bone fragment displacement, implant loosening, and subcutaneous irritation are common problems, with implant removal rates as high as 65%, demonstrating its inadequate mechanical control for dynamic compression stabilization.[9–18]

To enhance fixation stability, anterior locking plates have been increasingly adopted in clinical patellar reconstruction. This design provides direct anterior locking and compressive fixation[19–24]; however, given that the anterior surface of the patella has a highly complex curvature with substantial inter-individual variation, commercially available plates often require repeated intraoperative bending, fine-tuning, and locking by the surgeon to achieve proper conformity. In addition, the precision of conventional computer numerical control machining is limited when producing plates with multi-curvature surfaces, thin walls, or multi-axial screw trajectories, making fabrication challenging and costly and ultimately restricting the conformity and clinical operability of these implants.[19–23] Consequently, metal three-dimensional (3D) printing has emerged as an ideal solution, enabling accurate reconstruction of the patellar surface while integrating complex multi-functional design features.

An anatomically assembled thin bone plate (AATBP) fabricated using 3D printing has been proposed to improve the biomechanical performance of complex patellar fractures.[24,25] This plate incorporates a double-hook embracing structure and a ratchet-type height-adjustment mechanism, enabling adjustable fixation length based on patellar size and providing active compression. Finite element (FE) analysis and dynamic fatigue testing demonstrated that the AATBP obviously reduces fracture gap and bone stress while maintaining excellent stability under repeated loading. However, despite the use of 3D printing technology, the structural stiffness of the AATBP remains excessively high. Although this design offers strong operational stability, it limits implant light weighting and restricts flexible intraoperative adjustments. Therefore, the present study refines the previous design by introducing a topology-optimized, lightweight framework that reduces stiffness while preserving moderate elasticity and adaptive curvature, thereby improving clinical operability and achieving a balance between rigidity and adjustability.

Furthermore, clinical observations suggest that for patellar fractures located proximally in a transverse pattern or those that are highly comminuted,[14–18] relying solely on circumferential compression from the proximal and distal hooks, together with anterior screw fixation, may be insufficient. This limitation can result in displacement of the proximal fragment and uneven interfacial pressure. To address this mechanical deficiency, this study introduces a dual-compression design concept. Two micro distal-oriented fixation screws are incorporated into the proximal hook of the original AATBP. These screws extend distally to create a local bi-axial compression path. This design simultaneously generates downward pressure and inward clamping force, providing both circumferential and penetrating dual compression, thereby improving proximal fragment stability and shear resistance, particularly for proximal transverse and comminuted fracture patterns.

This study investigates the 3D-printed fabrication of a novel lightweight patellar fixation plate. Functional four-point bending static and fatigue tests were conducted to evaluate the structural rigidity, bending strength, and fatigue durability of the plate in accordance with the Food and Drug Administration (FDA) regulations and American Society for Testing and Materials (ASTM) F382 standards.[26] In parallel, the load-bearing capacity of proximal transverse and comminuted fractures within acceptable bone-healing gaps was evaluated under single-circumferential compression fixation and dual-compression fixation. Additionally, a biomechanical dynamic testing platform was utilized to replicate the repetitive loading conditions encountered during clinical knee extension. Dynamic fatigue tests were conducted to assess changes in fracture displacement and maximum reactive force under different fixation strategies, thereby determining the mechanical feasibility of the dual-compression patellar fixation plate.

2. Materials and methods

2.1. Novel bone plate design concept and finite element analysis

The novel 3D-printed patellar fixation plate is an extension and refinement of a previously published AATBP,[24,25] incorporating structural modifications based on the requirements of structural optimization and addressing unmet clinical needs for compression fixation. The AATBP was reconstructed using clinical patellar computed tomography morphology and features a modular configuration consisting of a proximal plate and a distal plate. These components were connected through a

ratchet-type compression adjuster, which allowed overall height adjustment according to patellar size. A dual-hook wrapping mechanism was included at both the proximal and distal ends to achieve circumferential coverage of the fracture margins and prevent slippage. The overall plate thickness was controlled at 1.6 mm to minimize subcutaneous irritation, and 0.6-mm-high conical bumps were incorporated on the posterior surface to enhance bone–implant friction and stability (Figure 1A).

The previously constructed computer-aided design (CAD) model of the patellar C3 comminuted fracture fixation AATBP and the associated ligaments/tendons were imported into ANSYS Workbench (version 22, Swanson Analysis, United States of America [USA]) for FE analysis. This analysis aimed to evaluate the mechanical behavior of the fixation under a standardized tensile loading condition. A quadratic 10-node tetrahedral solid element was used for meshing, resulting in 38,991 elements and 70,742 nodes (Figure 1A). To simulate contact behavior between bone–bone interfaces (fracture surfaces, friction coefficient = 0.45) and between the AATBP and bone (friction coefficient = 0.3), frictional contact elements reported in the literature were adopted. Cortical bone, cancellous bone, tendons, the AATBP, and fixation screws were all modeled as linear elastic and isotropic materials according to relevant literature.[24,25,27,28] The proximal (basal) nodes of the quadriceps tendon were fully constrained in all directions as boundary conditions. A tensile load of 150 N was applied along the longitudinal axis of the patellar tendon to simulate biomechanical testing conditions (Figure 1A).

Topology optimization was integrated with FE analysis to optimize the proximal plate structure.[29] The objective was to minimize compliance, i.e., maximize stiffness, while satisfying a 70% volume-retention constraint. This optimization aimed to achieve light weighting while maintaining an optimal distribution of structural material. The resulting topology maps indicated regions suitable for material removal, which were subsequently reconstructed in the CAD environment using SpaceClaim (version 22, Swanson Analysis, USA). Lateral wing structures were added to accommodate clinical micro-adjustments, allowing minor intraoperative shaping to match individual patellar curvatures on both sides (Figure 1A & B).

To provide proximal circumferential compression and alignment, holes were designed on both sides of the proximal plate at the hook platform locations, along the proximal–distal direction, to accommodate a locking screw (2.0 mm diameter, 17 mm length). The screw features continuous threading to lock its head into the hook platform, forming a dual-compression fixation pathway together with the screw originally inserted through the anterior curved surface of the plate. This mechanism provides dual-compression fixation for proximal transverse and comminuted fractures, thereby enhancing the overall stability of patellar fracture repair (Figure 2A).

The optimized plate was also evaluated via FE analysis using a C3 comminuted patellar fracture model, representing a clinically severe scenario, under identical loading and boundary conditions as the original AATBP. The optimized plate mesh model consisted of 110,855 elements and 159,971 nodes (Figure 1B). Bone maximum principal stress and plate von Mises stress were compared to evaluate differences in mechanical performance between the AATBP and the optimized plate.

2.2. Manufacturing of bone plate

The novel dual-compressive lightweight patellar bone plate was fabricated using metal 3D printing (additive manufacturing) technology. The components were produced using a selective laser melting (SLM) system, specifically the EOS M290 (EOS GmbH, Germany). The printing material used was a commercially available medical-grade Ti-6Al-4V alloy powder. Its chemical composition included titanium (balance), aluminum (5.5–6.5 wt%), vanadium (3.5–4.5 wt%), and controlled trace impurities such as oxygen (<0.13 wt%), carbon (≤0.08 wt%), and nitrogen (≤0.05 wt%). The particle size distribution ranged from 15 to 53 μm, meeting standard specifications for medical-grade powder bed fusion processing.[25] The SLM process employs a high-energy laser to selectively melt and solidify powder bed layers, enabling the fabrication of complex geometries and curved structures with high precision—an advantage particularly suited for orthopedic implants that require strict shape conformity.

For the manufacturing parameters, the laser power was set to 400 W, the scanning speed to 0.6 m/s, and the exposure time to 125 μs.[24,25,29] A layer thickness of 90 μm and a hatch spacing of 30 μm were selected to enhance component resolution and ensure dimensional stability. The overall manufacturing tolerance was controlled to approximately 30 μm. To minimize deformation caused by thermal accumulation, each plate was oriented along the edge of the patella contour, ensuring greater forming stability throughout the build process.

Post-processing was performed to improve surface quality after SLM fabrication. First, burrs were removed by hand, and then the surface was polished with a magnetic polishing system. The polishing medium consisted of stainless-steel pins (1 mm diameter, 3 mm length) that were operated at 2700 rpm. Residual powder and metallic debris were subsequently removed by ultrasonic cleaning, ensuring that surface cleanliness met clinical requirements.[24,25,29]

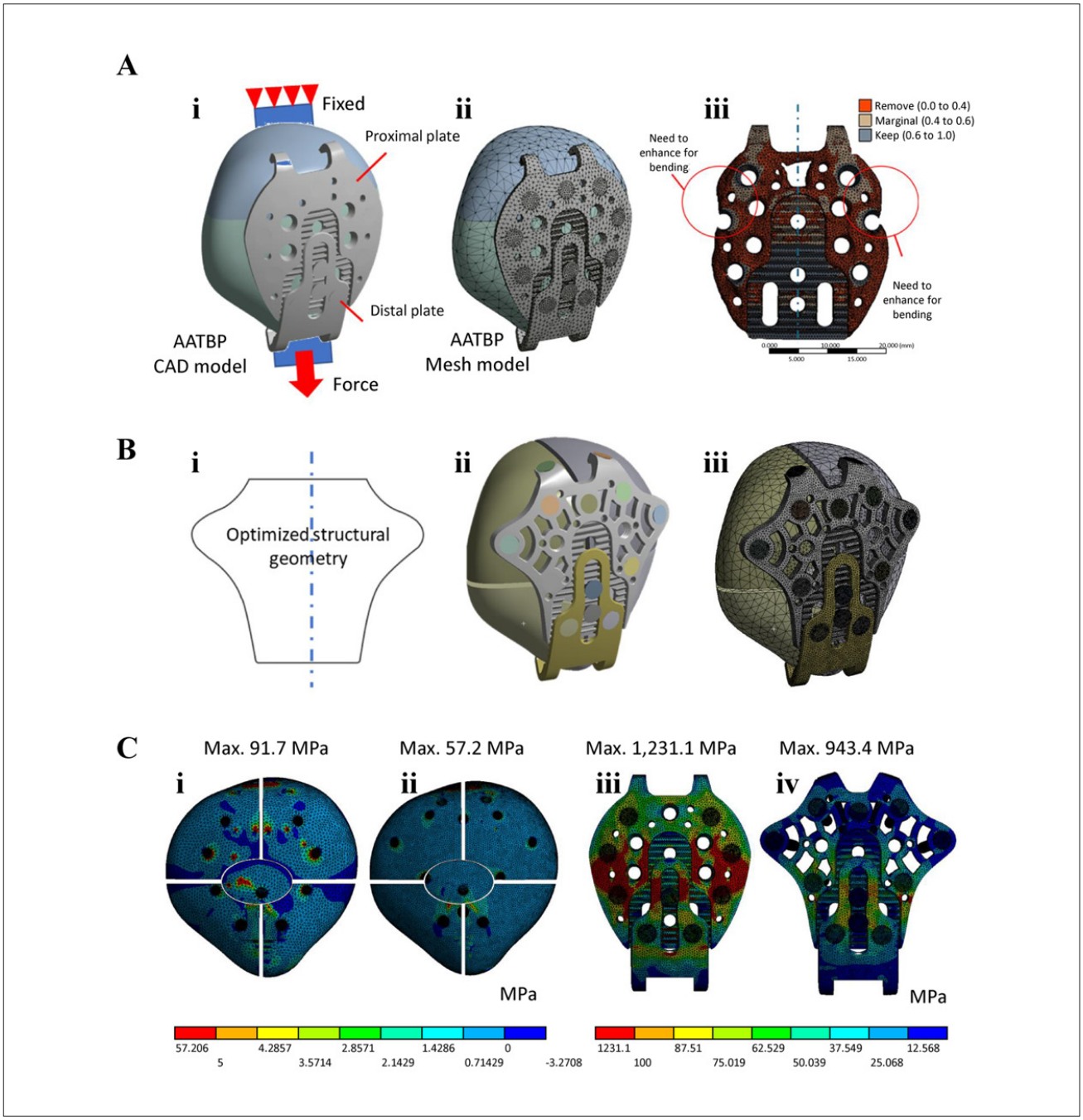

Figure 1. Topology-optimized and FE analysis of new plate. (A) Topology-optimized redesign of the proximal plate. The original anatomically assembled thin bone plate (AATBP) (i) computer-aided design (CAD) model and (ii) finite element (FE) mesh model are shown alongside the topology map, which indicates material retention and removal zones. (iii) The right part showed that critical load-bearing regions were preserved, and low-stress material was removed. (B) (i) Both lateral wing structures were added to accommodate minor intraoperative shaping. (ii) CAD and (iii) FE mesh models of the optimized plate, respectively. (C) (i) Bone principal stress patterns for AATBP and (ii) optimized plate, and corresponding maximum stress values. Plate von Mises stress patterns for (iii) AATBP and (iv) optimized plate, and corresponding maximum stress values.

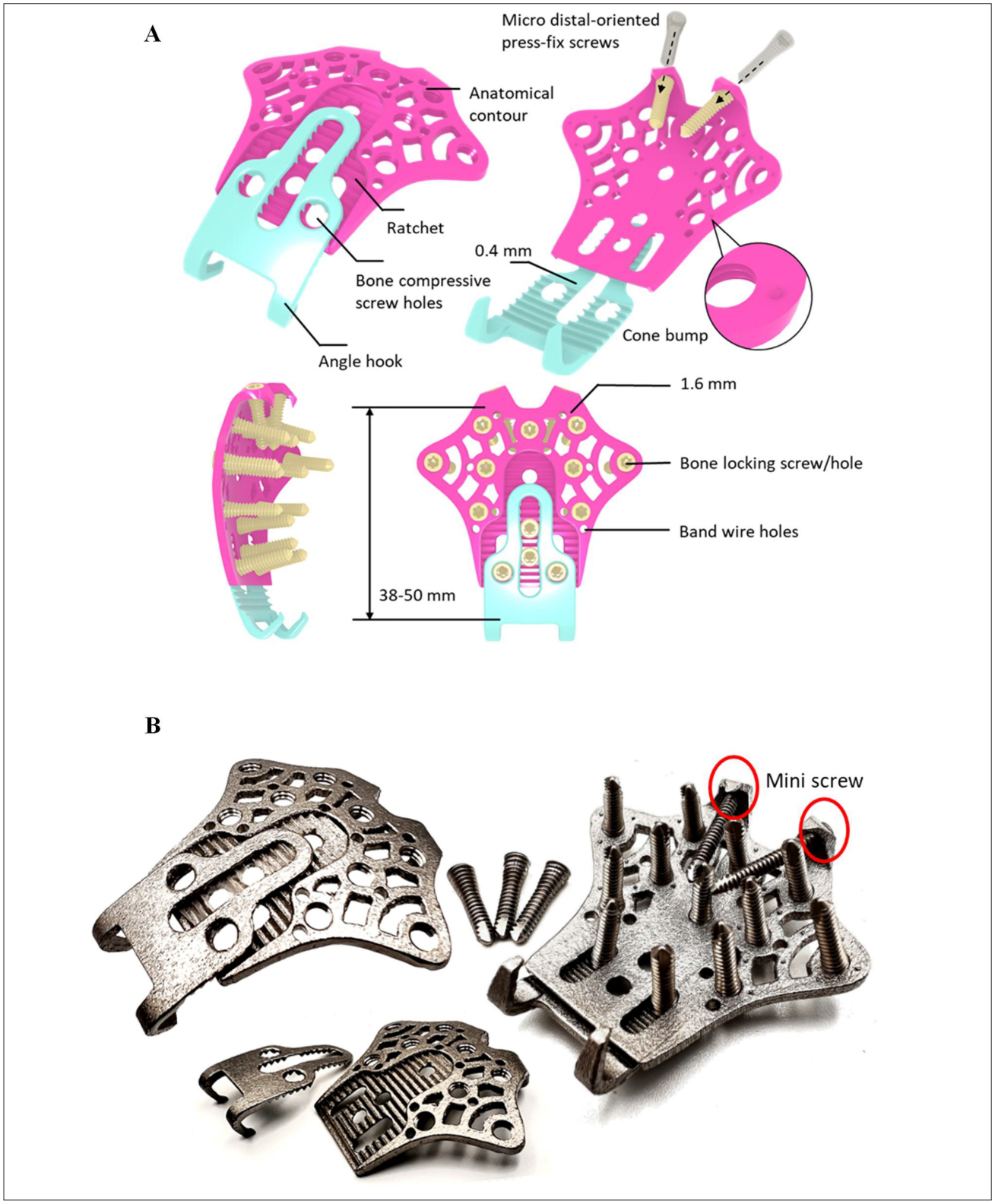

Figure 2. CAD and physical mode of the new patellar plate. (A) Final structural design of the topology-optimized patellar plate, featuring micro distal-oriented screws, ratchet adjustment mechanism, proximal and distal hooks, bone-contact cone bumps, and designated screw/wire holes. (B) Metal three-dimensional-printed components of the dual-compression patellar plate produced using selective laser melting.

To achieve the high geometric accuracy required for screw and wire holes, these features were not formed directly during the 3D printing process. Instead, their positions were predefined during the build and later finished by computer numerical control machining. This approach enabled the hole diameter tolerance to be maintained within 0.02 mm, ensuring compatibility with standard clinical screws. All of the holes were within clinically acceptable error limits (Figure 2B). This hybrid additive–subtractive manufacturing strategy combines the geometric freedom of 3D printing with the precision of conventional machining, resulting in a patellar plate that meets the functional and reliability standards required for clinical implantation.

2.3. Static and dynamic four-point bending tests of patellar plates

To provide a comprehensive mechanical reference for patellar plates used in skeletal fixation, static and dynamic four-point bending tests were conducted on the novel dual-compression lightweight patellar plate using an Instron 3000 testing machine (INSTRON, USA). The tests followed the ASTM F382-17 standard to evaluate bending stiffness, structural bending stiffness, bending strength, and fatigue strength.[26]

Since the patellar plate was a short and asymmetrical anatomical plate, it does not satisfy the standard roller-placement configuration specified in the regulation. Therefore, an alternative test setup was developed using rigid extension segments to effectively lengthen the plate and meet the geometric requirements of the four-point bending test. The patellar plate was secured to the customized extension segments at both ends using screws (Figure 3A). The extension segments were designed to avoid interfering with the actual deformation of the plate during bending. Both pairs of loading rollers and support rollers contacted only the extension segments rather than the plate itself, ensuring that the central region of the plate remained within the pure bending zone. In the test configuration, the span between the two loading rollers was set to a = 40 mm, and the distance between each loading roller and its adjacent support roller (loading span) was set to h = 40 mm, resulting in a total support span of 120 mm, consistent with the four-point bending geometry defined by ASTM F382. The roller diameter was 6 mm (Figure 3B).

Static testing was performed on three samples using a four-point bending fixture, with loading applied at a displacement rate of 0.05 mm/s until failure. For each test, the proof load (P), bending stiffness (K), and structural bending stiffness (EI_e) were calculated according to the standard, and the failure mode of each specimen was documented. The P was defined as the load corresponding to a 0.2% deviation from the linear region of the load–displacement curve, and the K was obtained from the slope of the linear portion of the load–displacement curve. The EI_e was calculated from the geometry of the four-point bending setup as shown in **Equation (1)**.

$$EI_e = \frac{(2h^3 + 3ha)Kh^2}{12} \quad (1)$$

Fatigue testing was conducted based on the P obtained from the static tests. Three maximum load levels were selected: 30% P, 25% P, and 15% P. Three specimens were tested at each load level. A sinusoidal cyclic load was applied at a constant frequency of 5 Hz, with the stress ratio (R-ratio) set to 0.1 (i.e., the minimum bending moment was 10% of the maximum). Each specimen was subjected to cyclic bending from initial loading until either an obvious fracture occurred or the cumulative cycle count reached 1×10^6 (runout), at which point the test was terminated. For each specimen, the maximum bending moment, termination cycle count, and failure mode and location were recorded to construct the moment–life (M–N) relationship.

2.4. Biomechanical static and dynamic tests

Common transverse patellar fractures (Arbeitsgemeinschaft für Osteosynthesefragen (AO) classification: 34-C1, denoted as C1) and complex comminuted five-part patellar fractures (AO classification: 34-C3, denoted as C3)[24,25] were selected as the test models. A 3D CAD model of the patella was reconstructed from skeletal computed tomography images. The model was simplified and segmented in CAD software (PTC Creo V6.0; PTC, USA) to simulate the two fracture types, leaving a passage for a 25-mm-wide polyester tension-band loop that simulated the quadriceps and patellar tendons (Figure 4A). Fabrication was performed using a 3D printer (Dimension 1200es SST; Stratasys, USA) with acrylonitrile–butadiene–styrene (ABS) copolymer (ABS-P430; Stratasys, USA) as the material. The novel dual-compression lightweight patellar plate could be adjusted via a ratchet mechanism to match the printed patellar height (approximately 40.0 mm). Fracture fragments were secured using corresponding hooks that passed through the straps. Before final fixation, the curvature of the plate was manually adjusted to match the anterior patellar surface as closely as possible. For C1 and C3 fractures, 2.4 × 12-mm locking screws (A Plus Biotechnology Co., Ltd., Taiwan) were inserted into the proximal plate. For dual-compression specimens, an additional locking screw was inserted on each side of the hook platform on the proximal plate. The screws were

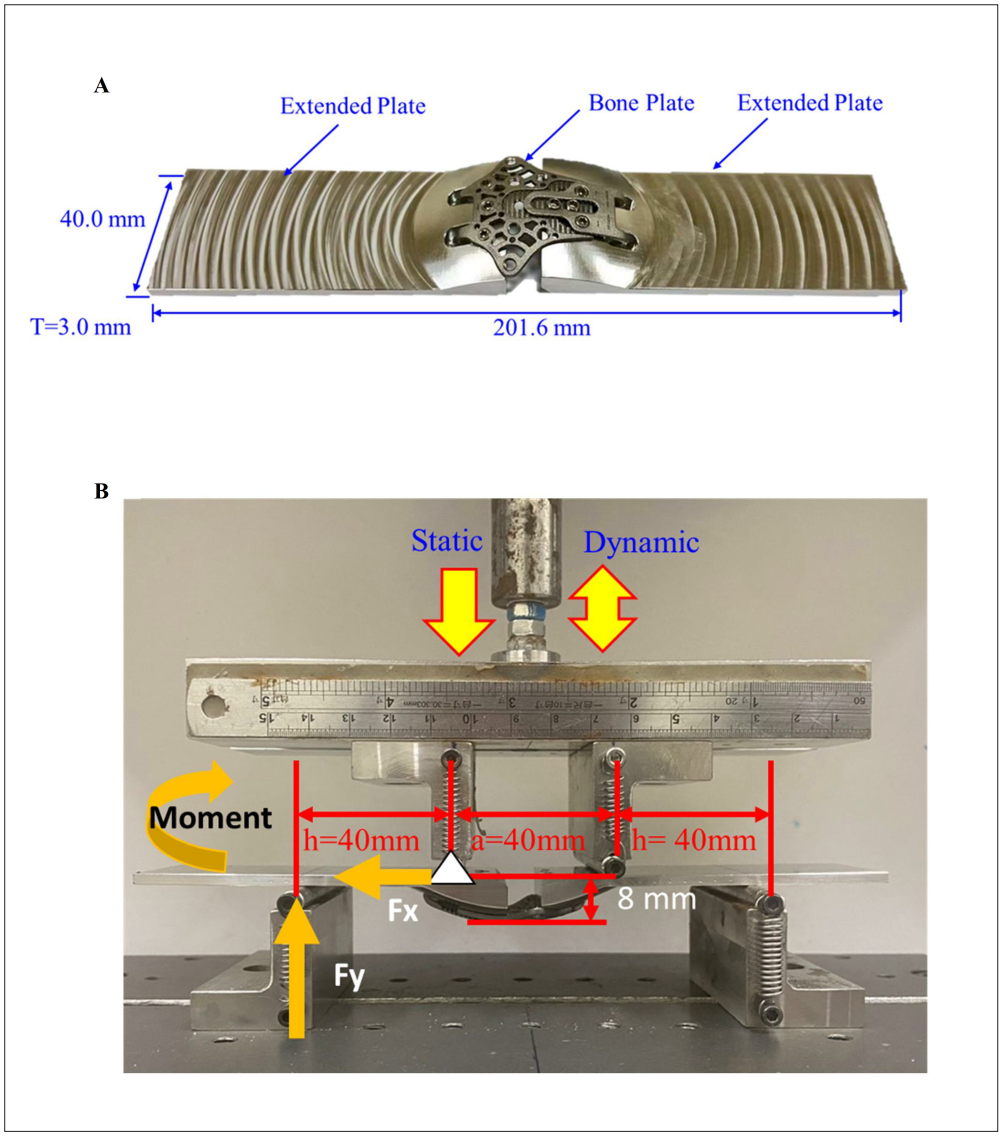

Figure 3. ASTM F-382 four-point bending testing. (A) Custom-designed extension plates used to satisfy American Society for Testing and Materials F382 standard four-point bending test geometry, enabling proper roller placement and establishing a pure bending region. (B) Four-point bending test setup showing applied forces, moment equilibrium calculations, loading span (h = 40 mm), total support span (120 mm), and the static proof-load determination (257.31 N).

evenly distributed with lateral symmetry to stabilize the fractured patella and effectively bypass the fracture gap (Figure 4B).

Static tensile failure tests were first conducted on both fracture types (C1 & C3) using single- and dual-compression fixation configurations. Three specimens were prepared for each test condition. Polyester tension bands simulating the quadriceps and patellar tendons at the proximal and distal ends were clamped to the upper and lower grips of the testing machine, respectively, ensuring the specimen's alignment and the loading direction. A measuring ruler was placed beside the specimen and parallel to the tension band to record crack opening on the medial and lateral sides after loading. The proximal tension band was then pulled upward at a rate of 3 mm/min until the medial or lateral crack opening exceeded 2 mm, at which point loading was stopped (Figure 4A). After removal, the medial and lateral crack openings were measured again using digital vernier calipers.

Twelve additional specimens were prepared for dynamic biomechanical testing, corresponding to two patellar fracture types and two fixation configurations

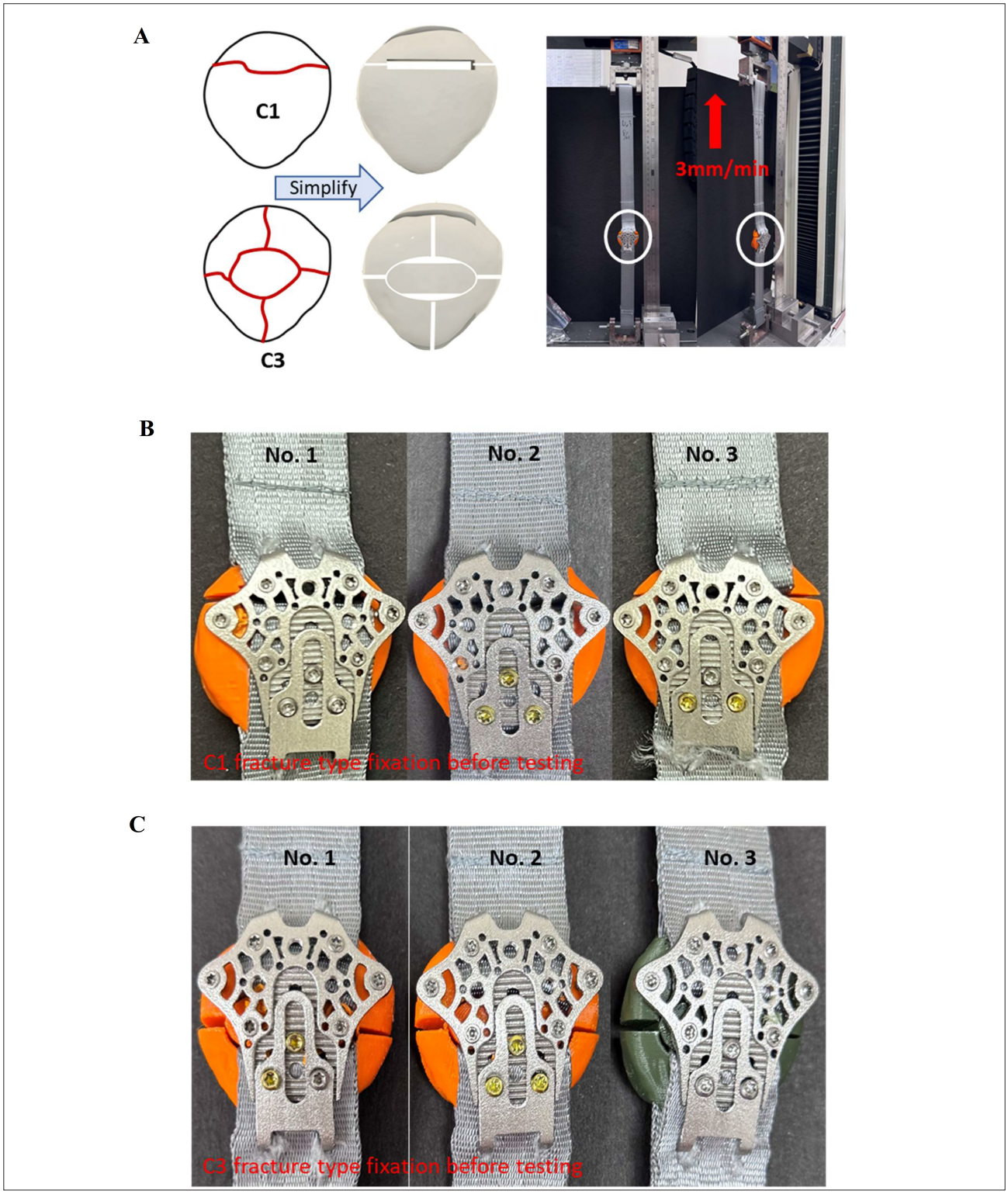

Figure 4. Static failure testing. (A) Computer-aided design-based reconstruction of C1 transverse and C3 comminuted patellar fractures and fabrication using acrylonitrile–butadiene–styrene three-dimensional printing. (B) Single and dual compression fixation configurations before static tensile loading for C1 fractures, showing specimen preparation. (C) Single and dual compression fixation configurations before static tensile loading for C3 fractures, showing specimen preparation. One sample exhibited a different color; however, the material composition was identical and did not affect the experimental results.

(single- and dual-compression) (n = 3 per group). All specimens were vertically clamped on the biomechanical testing platform previously developed by Liao *et al*[24,25] to simulate knee flexion at 90°. A femoral condyle model fabricated using ABS material via 3D printing served as the fulcrum, and a preload of 20 N was applied to ensure that the tension-band loop was fully stretched until the force–displacement curve entered the linear region (Figure 5A).

During dynamic testing, tensile loading was applied through polyester tension-band loops attached to the proximal end (quadriceps tendon) and distal end (patellar tendon). A vertical downward load of 15 kg (approximately 150 N) was added to simulate knee motion from 90° flexion to full extension at 0° (Figure 5A). Each cyclic loading test simulated the patellofemoral contact trajectory from 90° flexion (0 mm stroke) to 0° extension (50 mm stroke) at a constant speed of 5 mm/s. All specimens underwent 300 loading cycles, each controlled by a 50-mm position stroke. The relationship between quadriceps tendon force and flexion–extension displacement, measured using a force sensor, was recorded and plotted for each loading cycle (Figure 5A). Additionally, the fracture gap at the medial and lateral borders of each patella was measured using digital calipers before and after the final test cycle.

2.5. Statistical analysis

All recorded data in this study were organized and processed using Microsoft Excel (Microsoft 365, 2023; Microsoft, USA). Statistical comparisons among the five groups were performed using the Kruskal–Wallis test, due to the small sample size and non-normal data distribution, with analyses conducted using the Statistical Package for the Social Sciences software (version 22; IBM, USA).

3. Results

Figure 1A illustrates the geometric adjustments to material retention and removal based on the topology optimization results. Critical load-bearing regions were reinforced, while low-stress regions were removed. Lateral wing structures were added on both sides to accommodate minor intraoperative shaping, thereby completing the reconstruction and optimizing the implant design (Figure 1B). Figure 1C shows a comparison of FE analysis between AATBP and the new optimized plate, demonstrating that the maximum principal stress in the patella decreased from 91.7 MPa in the AATBP to 57.2 MPa in the new plate, indicating reduced stress transfer to the bone and a lower risk of secondary fracture or fixation failure. The plate's maximum equivalent stress also decreased from 1231.1 to 943.4 MPa, accompanied by a more uniform stress distribution. In contrast, the original AATBP exhibited a pronounced stress concentration in the central bridge region.

Figure 2A shows the final implant, redesigned according to the topology optimization results and manufactured using metal 3D printing. A locking screw can be inserted into the hook-platform region on both sides of the proximal plate, forming a "dual-compression" fixation pathway together with the screw originally inserted through the anterior plate surface. The right-side image of Figure 2B displays the actual screw-implantation configuration, confirming that no interference occurs between the newly added guide-screw hole and the original screw path, ensuring clinical feasibility and surgical convenience. The original AATBP structure weighed approximately 6 g, while the optimized bone plate weighed about 4.5 g, representing a reduction of roughly 25% (Figure 2B).

Figure 6Ai illustrates the load–displacement curve of the static four-point bending testing. The results showed that the mean (standard deviation) values of P, K, and EI_e were 257.31±5.40 N, 5.15±0.11 N/mm, and 1.10±0.01 N·m^2, respectively. The M–N curve from the dynamic fatigue four-point bending test is presented in Figure 6Aii. The results indicate that the plate cannot withstand one million loading cycles and fails under both 30% P and 25% P load levels (three specimens per group). Table 1 lists the relevant values. Figure 6B shows the appearance of the specimen after static testing. Figure 6C shows the fatigue–failure fracture morphology. Two failure modes were identified: Type I, characterized by an obvious fracture of the plate, and Type II, characterized by screw fracture without visible damage to the plate. The failure conditions of each specimen are summarized in Table 1.

Static biomechanical failure testing showed that, for both fracture types (C1 & C3), the dual-compression fixation method resulted in meaningfully higher failure loads—defined as a 2-mm increase in medial and lateral fracture-gap opening—than the single-compression method (Figure 7A). For both fracture types (C1 & C3), the higher failure-load values represent the dual-compression fixation method, and the lower values represent the single-compression method, reported as mean ± standard deviation. Specifically, for C1, the dual- and single-compression failure loads were 712 ± 31.51 N and 517.5 ± 29.05 N, respectively; for C3, the corresponding values were 253.75 ± 6.34 N and 205.25 ± 4.59 N (Figure 7B).

Dynamic biomechanical testing demonstrated that the maximum quadriceps-reaction force for all simulated conditions (Figure 5A) occurred within an extension-angle range of 62–66°. The average forces (**mean ± standard deviation**) for single- and dual-compression fixation were 293.92±38.4 N / 292±2.82 N for C1 and 262.13±22.63

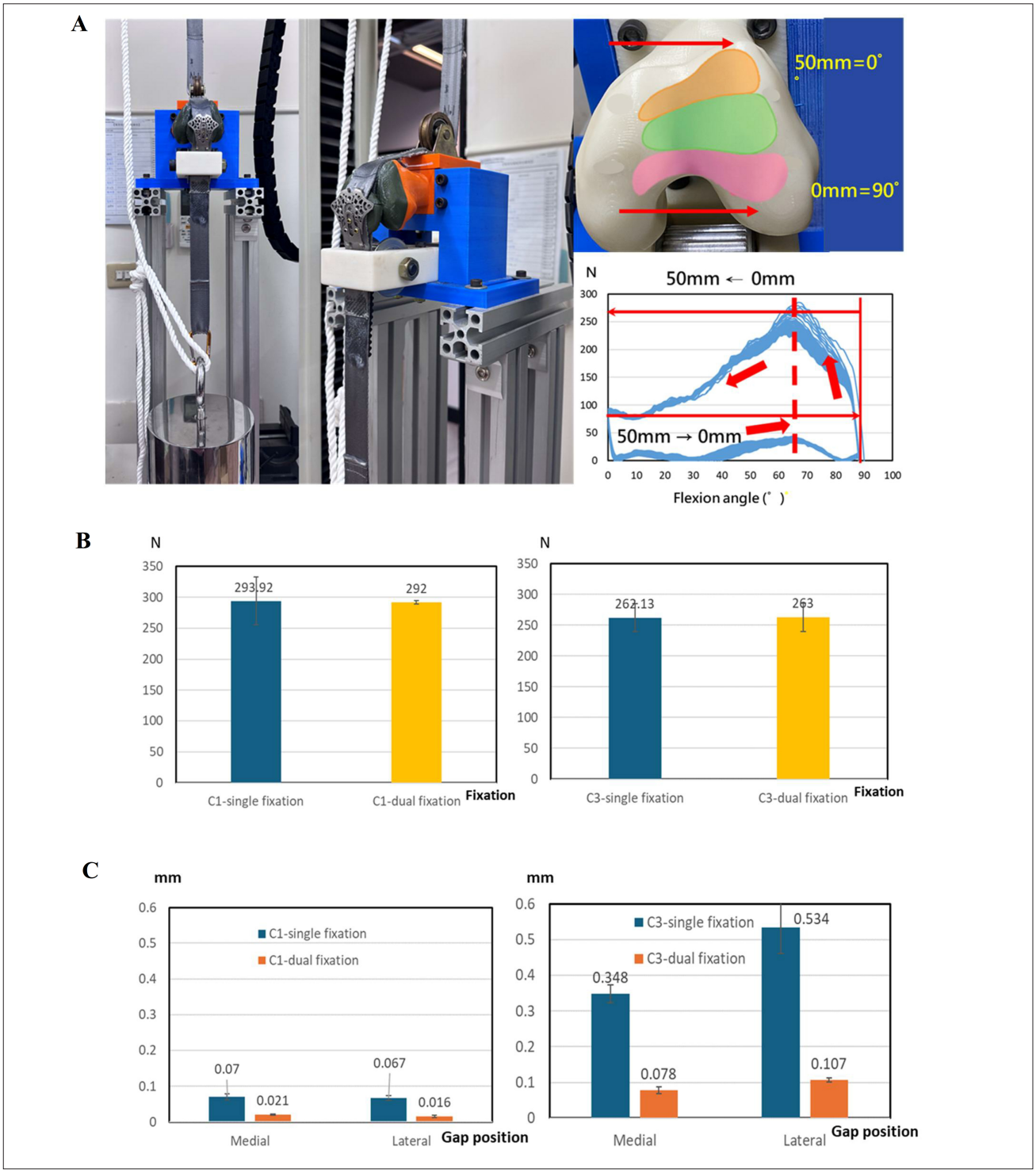

Figure 5. Dynamic test and results (A) Dynamic knee-extension biomechanical testing setup. Patella specimens were mounted at 90° knee flexion, and the femoral condyle model served as the fulcrum. The 50-mm stroke simulated patellofemoral motion from 90° flexion to 0° extension. (B) Quadriceps reaction forces for C1 and C3 fracture models under single- and dual-compression fixation, showing similar peak force ranges (62°–66° extension). (C) Interfragmentary gap measurements on medial and lateral fracture borders before and after dynamic loading, demonstrating significantly reduced micromotion under dual-compression fixation.

Table 1. Fatigue test results under different percentages of proof load

Sample	Percentage of proof load	Range of load (N)	Number of cyclic loads	Failure mode
4	30%	9.74–97.43	243,659	Type I
5	30%	9.74–97.43	19,770	Type II
6	30%	9.74–97.43	169,694	Type II
7	25%	8.12–81.19	666,352	Type II
8	25%	8.12–81.19	254,874	Type I
9	25%	8.12–81.19	690,677	Type II
10	15%	4.87–48.72	1,000,000	Pass
11	15%	4.87–48.72	1,000,000	Pass
12	15%	4.87–48.72	1,000,000	Pass

N / 263±22.9 N for C3 (Figure 5B), with no statistically significant differences (p>0.05).

Regarding interfragmentary gap measurements, both C1 and C3 fractures showed markedly smaller medial and lateral gap openings under dual-compression fixation than under single-compression fixation, and this improvement was statistically significant (p<0.05). For C1, the medial/lateral gaps under single vs. dual compression were 0.07 mm/0.067 mm (average 0.0685 mm) and 0.021 mm/0.016 mm (average 0.018 mm), respectively. The corresponding gaps for C3 were 0.348 mm/0.534 mm (average 0.441 mm) and 0.078 mm/0.107 mm (average 0.0925 mm) (Figure 5C). Additionally, C1 consistently exhibited smaller medial and lateral gaps than C3, regardless of the fixation configuration.

4. Discussion

This study reconfigured the material distribution of the anterior patellar plate through topology optimization to address the excessive stiffness of the original AATBP while preserving the structural integrity required for patellar fixation. The primary objective was to allow slight intraoperative bending without compromising the essential load-bearing framework. By applying a topology optimization algorithm constrained by a 70% volume fraction, material was preferentially retained along the primary tension and compression transmission paths in the bending core region, while low-stress peripheral material was removed to reduce overall stiffness and weight.

The 70% volume constraint was not arbitrarily selected; instead, it was determined based on convergence behavior and clinical design constraints. Since the original AATBP includes predetermined screw holes at fixed clinical positions, excessive material removal around these regions led to numerical instability and unrealistic geometries. An initial optimization attempt with 60% volume retention failed to converge, likely due to insufficient load-transfer pathways surrounding the constrained screw-hole regions. In contrast, stable convergence was achieved at a 70% volume retention rate, which was therefore selected as the lowest feasible and convergent constraint.

As a result, the plate mass was reduced from approximately 6.0 g for the original AATBP to 4.5 g for the optimized design, representing a 25% reduction in weight. In addition, lateral wing structures were incorporated to form locally thin-walled regions, enabling minor surgical contouring while maintaining the mechanical integrity of the core load-bearing region. Under identical loading and boundary conditions, FE analysis using a C3 comminuted patellar fracture model further demonstrated the mechanical advantages of the optimized design compared with the original AATBP. The maximum principal stress in the patella decreased from 91.7 MPa to 57.2 MPa, indicating reduced stress transfer to the bone and a lower risk of secondary fracture or fixation failure. The maximum equivalent stress in the plate also decreased from 1,231.1 MPa to 943.4 MPa, accompanied by a more uniform stress distribution, whereas the original AATBP exhibited pronounced stress concentration in the central bridge region. Collectively, these results confirm that the optimized AATBP achieved a 25% weight reduction while maintaining—and in some aspects improving—its mechanical performance, thereby supporting the core claim that the plate can be lightened without compromising structural stability.

Regarding the concept of proximal enhanced compression, this study proposed a reinforced dual-compression mechanism to enhance shear control and fragment coaptation. Two miniature locking screws were therefore added to the proximal hook platform. The compressive force generated by these screws provides additional axial compression and inward clamping on the proximal fragments, reducing the likelihood of

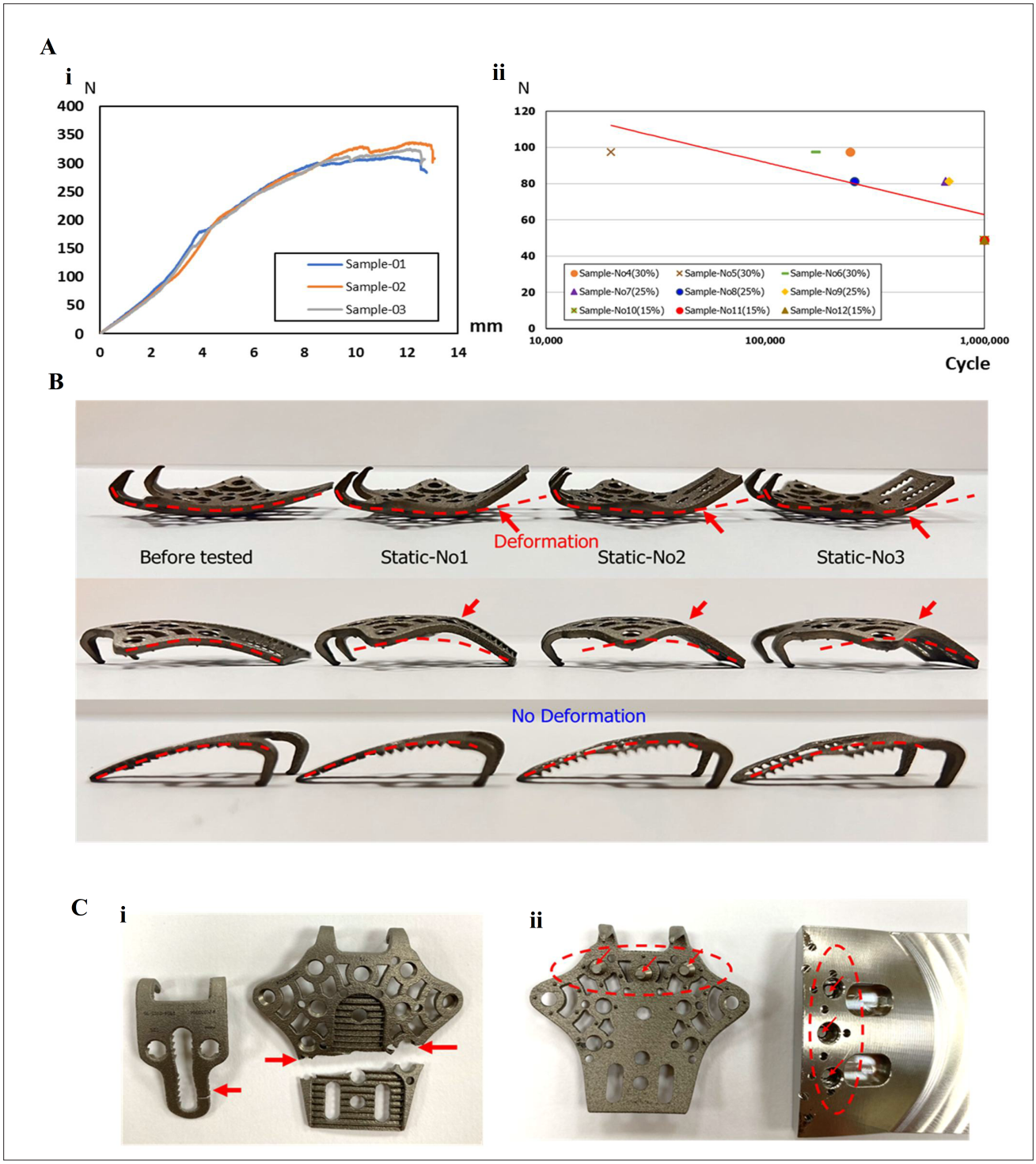

Figure 6. Results of four-point bending test. (A) Load–displacement curves and S–N (moment–life) fatigue curves from ASTM F382 testing. The plate failed before 1×10^6 cycles at 25% proof load and 30% proof load. (B) Static bending deformation patterns for three specimens, compared with the undeformed plate prior to testing. (C) Two fatigue-failure modes: (i) Type I—fracture of the plate at the topology-optimized transition zone; (ii) Type II—locking-screw fracture without visible plate damage.

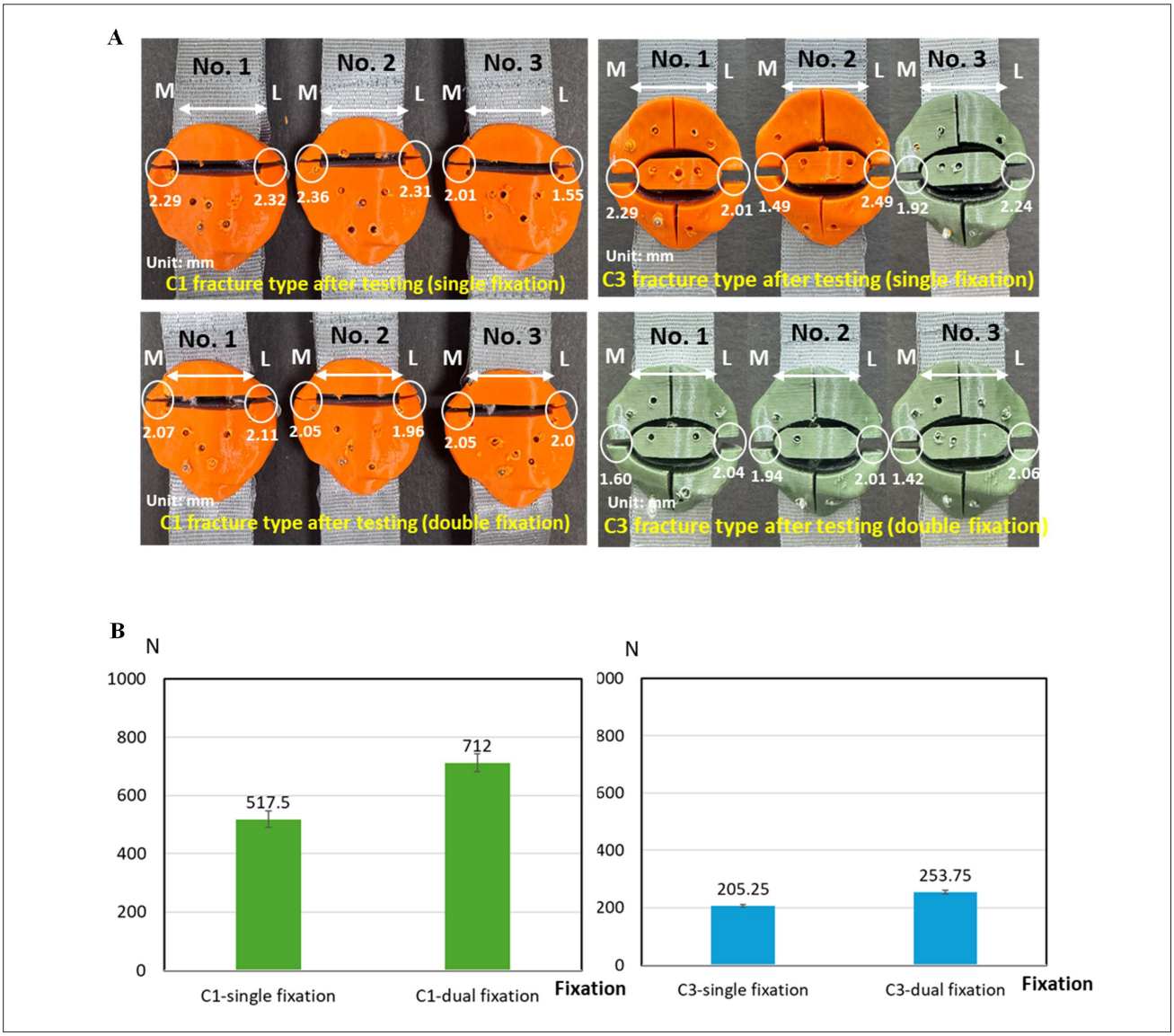

Figure 7. Results of dynamic biomechanical test. (A) Static tensile failure patterns for C1 and C3 fractures under single- and dual-compression fixation, showing medial and lateral gap openings at the 2-mm failure criterion. Some samples exhibited different colors; however, the material composition was identical and did not affect the experimental results. (B) Failure loads for C1 and C3 fractures, indicating significantly (*p<0.05) higher load-bearing capacity with dual-compression fixation compared with single-compression fixation.

slippage or valgus displacement under tensile loading. Static biomechanical tensile testing confirmed that, for both C1 and C3 fractures, dual compression resulted in a substantially higher failure load than single compression.

Dynamic knee-extension testing further demonstrated that dual compression significantly reduced micromotion at the fracture interface during functional loading. Using a dynamic platform capable of reproducing patellar sliding, rotation, and tension changed from 90° to 0° of knee extension, deformation across the medial and lateral fracture lines was quantified. The results showed that dual compression produced markedly reduced fracture-gap opening with improved bilateral symmetry; in C3 fractures, the gap decreased dramatically from 0.348–0.534 mm to 0.078–0.107 mm for the medial-lateral side. Literature indicates that maintaining interfragmentary micromotion within 0.2–1.0 mm provides a mechanically favorable environment for endochondral ossification and promotes stable bone healing.[30,31] Therefore, the dual-compression design demonstrated in this study provides an effective strategy for improving the biological healing environment without increasing quadriceps reaction

forces, confirming that the construct does not impose excessive mechanical constraint.

In this study, a comprehensive dynamic biomechanical comparison was further conducted among the topology-optimized single- and dual-compression plates, the previous AATBP design, and a commercially inspired anterior plate (ASP).[25] In terms of quadriceps reaction force, ASP exhibited the highest peak values in both C1 and C3 fracture models (334.5 N & 260.6 N, respectively), indicating the least stable force transmission behavior. In contrast, the AATBP demonstrated the lowest reaction forces (238.1 N for C1 & 198.3 N for C3), reflecting its high structural stiffness and efficient load transmission. The topology-optimized plates showed intermediate reaction forces between ASP and AATBP, with peak values of 293.92 N and 262.13 N for the single- and dual-compression configurations in C1 fractures, and 292 N and 263 N, respectively, in C3 fractures. These values were significantly ($p<0.05$) higher than those of AATBP (C1: $p = 0.045/0.010$; C3: $p = 0.006/0.006$), indicating a redistribution of load-sharing pathways rather than a reduction in fixation capability.

Unlike quadriceps reaction force, fracture gap displacement represents a more direct and clinically relevant indicator of fixation stability. As summarized in Table 2, C1 fractures showed a progressive reduction in average fracture gap in the order of ASP, AATBP, single-compression, and dual-compression fixation, with the dual-compression design achieving the smallest gap (0.018 mm) and thus the highest stability among all configurations. In C3 comminuted fractures, the AATBP exhibited an extremely small fracture gap (0.0274 mm), which can be attributed to its inherently high structural stiffness. However, even under these highly unstable and clinically challenging conditions, the topology-optimized dual-compression design limited fracture gap displacement to only 0.0925 mm, representing a substantial improvement compared with the ASP plate (1.93 mm). These findings demonstrate that the dual-compression configuration provides superior fragment control and shear stability relative to the commercial reference. Overall, this direct comparison confirms that the topology-optimized dual-compression plate not only advances the structural design beyond the previous AATBP but also delivers superior biomechanical fixation performance in fracture scenarios associated with the greatest clinical instability.

Four-point bending static and fatigue tests revealed that, although the plate structure still exhibited localized high-stress concentration, its overall mechanical performance satisfied baseline safety requirements. According to the ASTM F382 results, the static P, K, and EI_e all met the criteria for metallic bone plates. Under cyclic loading, the plate successfully withstood more than one million cycles without failure at 15% P, meeting FDA fatigue performance requirements for long-term use. However, the plate failed to reach one million cycles at higher load levels of 25% P and 30% P. According to the standard, failure includes not only a complete fracture but also visible crack formation or excessive displacement. Therefore, in our study, any noticeable cracking of the plate or screw was considered a failure to meet the 1×10^6 cycle requirement at that load level. Two distinct failure modes were found for all samples. Type I failure was characterized by fatigue crack initiation in the proximal–central transition region, where the topology-optimized material removal ratio was relatively high, suggesting that the local section modulus and effective EI_e in this area remained insufficient. Type II failure involved

Table 2. Comparison of medial and lateral fracture gap displacement in C1 and C3 fractures

Fracture	Image	ASP	AATBP	Single fixation	Dual fixation
C1		1.233±0.641/0.949±0.917	0.257±0.33/0.110±0.156	0.07±0.0081/0.067±0.0072	0.02±0.0015/0.016±0.0032
Average		1.091	0.2935	0.0685	0.018
C3		1.697±0.66/2.163±1.03	0.002±0.221/0.025±0.414	0.348±0.0249/0.519±0.0604	0.078±0.0098/0.107±0.0061
Average		1.93	0.027	0.4335	0.0925

Note: All data are presented as mean ±standard deviation of medial/lateral components. C1 fracture: ASP>AATBP>Single>Dual; C3 fracture: ASP>Single>Dual>AATBP.

Abbreviations: AATBP, anatomically assembled thin bone plate; ASP, commercially inspired anterior plate.

fracture of the locking screw due to excessive shear loading, indicating that load transfer between the plate and screws was not yet optimally balanced.

The observed fatigue behavior can be attributed to both structural and material factors. Although topology optimization effectively reduces weight by removing material from low-stress regions, it may also introduce stress risers around screw holes and locally thinned sections that reach fatigue limits earlier under high cyclic loads. In addition, the metal 3D-printed Ti-6Al-4V plates in this study did not undergo post-processing treatments such as hot isostatic pressing or annealing, which are known to reduce internal porosity and improve fatigue resistance. Consequently, the fatigue performance at higher load levels is expected to be lower than that of wrought or post-processed components, as reported in previous studies of additively manufactured implants. From a clinical perspective, the 15% *P* condition represents a conservative estimate of long-term postoperative loading under appropriate rehabilitation protocols, whereas the 25% *P* and 30% *P* conditions serve as stress–test scenarios, reflecting unexpected or extreme loading events, such as noncompliance, accidental falls, or high patient activity. These findings not only clarify the fatigue performance envelope of the current design but also provide clear directions for next-generation optimization, including reinforcing the proximal–central transition region, thickening selected struts, and redesigning screw-hole geometry to reduce stress concentration and enhance fatigue durability.

It is worth noting that the ASTM F382 testing completed in this study is not only scientifically meaningful but also represents a key milestone for future commercialization. Patellar fixation plates are classified as Class II medical devices, which do not require animal implantation studies but must pass the four-point bending static and fatigue tests specified in ASTM F382 to demonstrate adequate safety under functional loading conditions. In the static four-point bending test, the *P* was 257.31 N (*y*-direction). Using the left load application point as the fulcrum and applying the principle of moment equilibrium, F_y = 257.31/2 N, therefore:

$$128.655\ \text{N} \times 40\ \text{mm} = F_x \times 8\ \text{mm} \quad (2)$$

the reaction force at the fulcrum was calculated to be approximately 618.275 N (*x*-direction: F_x) (Figure 3B). This value exceeds the 517.5 N required in biomechanical tensile testing to produce an interfragmentary gap of more than 2 mm, thereby confirming that the plate provides sufficient structural strength. Furthermore, the test results provide comprehensive data on *K*, EI_e, fatigue life, and failure modes, all of which serve as important technical references for the FDA's safety evaluation. These data also offer objective benchmarks for comparison with existing commercially available patellar fixation plates.

The use of ABS 3D-printed patellar models for biomechanical testing was motivated by the advancement of 3D printing technology; consequently, many biomechanical studies now employ 3D-printed bone analogs to evaluate trend-level mechanical differences under highly controlled conditions.[25,32] The primary advantage of this approach is the ability to maintain identical geometry and material properties across specimens, thereby minimizing biological variability that could otherwise obscure fixation-related effects. Consistent with this rationale, the ABS 3D-printed patellae used in this study were not intended to replicate the absolute mechanical behavior of real bone. Instead, they were selected to provide a highly uniform testing substrate, ensuring that differences in fixation design (e.g., C1 vs. C3, single vs. dual compression) constituted the dominant source of mechanical variation. In contrast, natural patellae exhibit substantial inter-individual variability in cortical thickness and cancellous bone density, which could introduce experimental noise exceeding the true mechanical effects of the fixation constructs and thereby reduce the statistical power of between-group comparisons.

Although the elastic modulus and fracture toughness of ABS differ from those of human cortical and cancellous bone and may affect the absolute magnitudes of fracture gap or micromotion, all specimens in this study were fabricated using identical ABS material, printing parameters, and density, ensuring that relative mechanical differences and trends between fixation designs remain valid. To further verify the physiological relevance of these trends, an additional FE analysis using human bone material properties was performed for the single-fixation configuration, demonstrating that the optimized plate exhibited a larger average fracture gap (0.207 mm) than the AATBP (0.187 mm), consistent with the ABS experimental results.

The dynamic testing platform used in this study is a well-established and validated model for comparative patellar biomechanics. The applied 150 N compressive load and single-plane sliding trajectory were adapted from widely accepted protocols in the literature and have also been validated in our previous studies.[24,25] This setup was intentionally designed to provide a highly standardized and reproducible dynamic environment for comparing the relative mechanical performance of different fixation constructs, rather than to replicate the full 3D patellofemoral motion.

Although physiological patellofemoral mechanics involve multi-directional loading, incorporating such complexity would markedly reduce test repeatability and increase inter-specimen variability. While a simplified two-dimensional loading model may underestimate absolute fracture gap magnitude, all constructs—including both fracture types (C1 & C3) and fixation strategies (single & dual compression)—were tested under identical loading and kinematic conditions. This ensures that the observed between-group differences remain valid and reproducible. Future studies using cadaveric patellae and whole-joint biomechanical models under more physiologically representative 3D loading conditions are warranted to further validate the clinical applicability of the dual-compression design.

5. Conclusion

This study developed a topology-optimized, metal 3D-printed dual-compression patellar plate and demonstrated its mechanical feasibility. The optimized design preserved key load-bearing paths while reducing excessive stiffness, and the manufactured plate met ASTM F382 static requirements with runout at 15% *P* in fatigue testing. Two fatigue-failure modes—plate transition-zone cracking and locking-screw fracture—were identified, highlighting areas for structural reinforcement. Static tensile and dynamic knee-extension tests further showed that the dual-compression mechanism significantly improved fragment stability and reduced interfragmentary micromotion, especially in comminuted fractures, without increasing quadriceps reaction force. Overall, the dual-compression plate provides enhanced fixation stability and effective micromotion control, supporting its potential as an improved solution for challenging patellar fractures.

Acknowledgments

None

Funding

This study is supported in part by NSTC project 113-2622-E-A49 -027 and 114-2923-E-A49 -014 -MY2 Taiwan.

Conflict of interest

No potential conflict of interest was reported by the author(s).

Author contributions

Conceptualization, Methodology: Chi-Yang Liao
Methodology, Investigation: Shao-Fu Huang
Methodology: Hsuan-Wen Wang, Ya-Han Chan
Software: Yu-Pin Yang
Investigation, Conceptualization, Writing-Reviewing and Editing: Chun-Li Lin

Ethics approval and consent to participate

Not applicable.

Consent for publication

Not applicable.

Availability of data

The data that support the findings of this study are available from the corresponding author upon reasonable request.

References

1. Schmidt V, Möller Rydberg E, Krause M, Wolf O. Patient-reported outcomes following patella fractures: a nationwide observational study of 8,726 patients from the Swedish Fracture Register. *Bone Jt Open***.** 2025;6(9):1080-1089. doi: 10.1302/2633-1462.69.BJO-2025-0141.R1
2. Larsen P, Court-Brown CM, Vedel JO, Vistrup S, Elsoe R. Incidence and epidemiology of patellar fractures. *Orthopedics***.** 2016;39(6):e1154-e1158. doi: 10.3928/01477447-20160811-01
3. Larsen P, Vedel JO, Vistrup S, Elsoe R. Long-lasting hyperalgesia is common in patients following patella fractures. *Pain Med***.** 2018;19(3):429-437. doi: 10.1093/pm/pnx144
4. Fehske K, Berninger MT, Alm L, *et al*. Current treatment standard for patella fractures in Germany. *Unfallchirurg***.** 2021;124(10):832-838. doi: 10.1007/s00113-020-00939-8
5. Gwinner C, Märdian S, Schwabe P, Schaser KD, Krapohl BD, Jung TM. Fractures of the patella: current concepts review. *GMS Interdiscip Plast Reconstr Surg DGPW***.** 2016; 5:Doc01. doi: 10.3205/iprs000080
6. Singh S, Surana R, Rai A, Sharma D. Outcome analysis of fixed angle locking plate in patella fractures: a single centre experience from North India. *Indian J Orthop***.** 2021;55(3):655-661. doi: 10.1007/s43465-020-00302-4
7. Neumann-Langen MV, Sontheimer V, Näscher J, Izadpanah Z, Schmal H, Kubosch EJ. Incidence of postoperative complications in patellar fractures related to different osteosynthesis procedures. *BMC Musculoskelet Disord***.** 2023;24(1):871. doi: 10.1186/s12891-023-06998-3
8. Stoffel K, Zderic I, Pastor T, *et al*. Anterior variable-angle locked plating versus tension band wiring of simple and

complex patella fractures: a biomechanical investigation. *BMC Musculoskelet Disord*. 2023;24(1):279. doi: 10.1186/s12891-023-06394-x

9. Hung LK, Chan KM, Chow YN, Leung PC. Fractured patella: operative treatment using the tension band principle. *Injury*. 1985;16(5):343-347. doi: 10.1016/0020-1383(85)90144-5
10. Dy CJ, Little MTM, Berkes MB, *et al*. Meta-analysis of re-operation, nonunion, and infection after open reduction and internal fixation of patella fractures. *J Trauma Acute Care Surg*. 2012;73(4):928-932. doi: 10.1097/TA.0b013e31825168b6
11. Larsen P, Rathleff MS, Østgaard SE, Johansen MB, Elsøe R. Patellar fractures are associated with an increased risk of total knee arthroplasty: a matched cohort study with 14.3-year follow-up. *Bone Joint J*. 2018;100-B(11): 1477-1481. doi: 10.1302/0301-620X.100B11.BJJ-2018-0472.R1
12. Garner MR, Homcha B, Cowman T, Goss M, Reid JS, Lewis GS. Transverse patella fracture fixation: a cadaveric biomechanical comparison of cannulated screws and anterior tension band versus low-profile multiplanar mesh plating. *Injury*. 2024;55(6):111574. doi: 10.1016/j.injury.2024.111574
13. Gibert S, Kowaleski MP, Matthys R, Nützi R, Serck B, Boudrieau RJ. Biomechanical comparison of pin and tension-band wire fixation with a prototype locking plate fixation in a transverse canine patellar fracture model. *Vet Comp Orthop Traumatol*. 2016;29(1):20-28. doi: 10.3415/VCOT-15-07-0115
14. Wild M, Fischer K, Hilsenbeck F, Hakimi M, Betsch M. Treating patella fractures with a fixed-angle patella plate: a prospective observational study. *Injury*. 2016;47(8):1737-1743. doi: 10.1016/j.injury.2016.06.018
15. Siljander MP, Vara AD, Koueiter DM, Wiater BP, Wiater PJ. Novel anterior plating technique for patella fracture fixation. *Orthopedics*. 2017;40(4):e739-e743. doi: 10.3928/01477447-20170615-02
16. Lee KH, Lee Y, Lee YH, Cho BW, Kim MB, Baek GH. Biomechanical comparison of three tension band wiring techniques for transverse fracture of patella. *J Orthop Surg (Hong Kong)*. 2019;27(3):2309499019882140. doi: 10.1177/2309499019882140
17. Wagner FC, Neumann MV, Wolf S, *et al*. Biomechanical comparison of a 3.5-mm anterior locking plate to cannulated screws with tension band wiring in comminuted patellar fractures. *Injury*. 2020;51(6):1281-1287. doi: 10.1016/j.injury.2020.03.030
18. Kfuri M, Escalante I, Schopper C, *et al*. Comminuted patellar fractures: the role of biplanar fixed-angle plate constructs. *J Orthop Translat*. 2021;27:17-24. doi: 10.1016/j.jot.2020.09.003
19. Berninger MT, Frosch KH. Change in the treatment of patellar fractures. *Unfallchirurgie (Heidelb)*. 2022;125(7):518-526. doi: 10.1007/s00113-022-01167-y
20. Moore TB, Sampathi BR, Zamorano DP, Tynan MC, Scolaro JA. Fixed angle plate fixation of comminuted patellar fractures. *Injury*. 2018;49(6):1203-1207. doi: 10.1016/j.injury.2018.03.030
21. Wurm S, Augat P, Bühren V. Biomechanical assessment of locked plating for fixation of patella fractures. *J Orthop Trauma*. 2015;29(9):e305-e308. doi: 10.1097/BOT.0000000000000309
22. Ellwein A, Lill H, DeyHazra RO, Smith T, Katthagen JC. Outcomes after locked plating of displaced patella fractures: a prospective case series. *Int Orthop*. 2019;43(12): 2807-2815. doi: 10.1007/s00264-019-04337-7
23. Elsoe R, Thorninger R, Severinsen R, *et al*. Tension band versus locking plate fixation for patella fractures: protocol for a randomized controlled trial. *Dan Med J*. 2024;71(5):A12230753. doi: 10.61409/A12230753
24. Liao CY, Huang SF, Tsai WC, Zeng YH, Li CH, Lin CL. Biomechanical evaluation of an anatomical bone plate assembly for thin patella fracture fixation fabricated by titanium alloy 3D printing. *Int J Bioprint*. 2023;9(6):0117. doi: 10.36922/ijb.0117
25. Liao CY, Huang SF, Tsai WC, *et al*. Biomechanical comparison of traditional and 3D-printed titanium alloy anatomical anterior plating under three patellar fracture conditions. *Virtual Phys Prototyp*. 2024;19(1):e2404982. doi: 10.1080/17452759.2024.2404982
26. ASTM International. *ASTM F382-24: Standard Specification and Test Method for Metallic Bone Plates*. West Conshohocken, PA: ASTM International; 2024. doi: 10.1520/F0382-24
27. Chang CW, Chen CH, Li CT, *et al*. Role of an additional third screw in fixation of transverse patellar fracture with two parallel cannulated screws and anterior wire. *BMC Musculoskelet Disord*. 2020;21(1):752. doi: 10.1186/s12891-020-03744-x
28. Chen CH, Chen YN, Li CT, Chang CW, Chang CH, Peng YT. Roles of the screw types, proximity and anterior band wiring in the surgical fixation of transverse patellar fractures: a finite element investigation. *BMC Musculoskelet Disord*. 2019;20(1):99. doi: 10.1186/s12891-019-2474-7
29. Wang HW, Chen CH, Chen KH, Zeng YH, Lin CL. Designing a 3D-printed medical implant with macrostructural topology and microbionic lattices: a novel wedge-shaped spacer for high tibial osteotomy and biomechanical study. *Int J Bioprint*. 2024;10(1):1584.

doi: 10.36922/ijb.1584

30. Wen J, Zeng Y, Su S, *et al*. Magnesium degradation-induced variable fixation plates promote bone healing in rabbits. *J Orthop Traumatol***.** 2024;25:56.
doi: 10.1186/s10195-024-00803-0

31. Huxman C, Lewis G, Armstrong A, Updegrove G, Koroneos Z, Butler J. Mechanically compliant locking plates for diaphyseal fracture fixation: a biomechanical study. *J Orthop Res***.** 2025;43(1):217-227.
doi: 10.1002/jor.25968

32. Nägl K, Reisinger A, Pahr DH. The biomechanical behavior of 3D-printed human femoral bones based on generic and patient-specific geometries. *3D Print Med***.** 2022;8(1):35.
doi: 10.1186/s41205-022-00162-8